Geochemical Perspectives Letters

Mercury isotopes in North Pacific sediments reveal vegetation expansion in warm climates

Y. Qu, R. Sun, S. Li, Y. Yang, R. Hu, X. Yang, J. Zheng, X. Chen, Q. Hong, Z. Cao, D. Shi, J. Chen, T. Chen

Supplementary Information

The Supplementary Information includes:

- Sample Information, Methods, and Details on Data
- Tables S-1 to S-3
- Figures S-1 to S-4
- Supplementary Information References

Sample Information, Methods, and Details on Data

Sample information

The sampling site of this study is the Central High of the Shatsky Rise under the modern Kuroshio Extension. The gravity core KEC (36.13 °N, 158.21 °E, water depth of 3346 m) provides the record since the Last Glacial Maximum (LGM, approximately 26 ka). The age model is adopted from Yang *et al*. (2024), which is based on radiocarbon dating of planktonic foraminifera. Age-depth modelling is performed using the *Undatable* software (Lougheed and Obrochta, 2019), with the Marine20 radiocarbon calibration curve. Reservoir age corrections were applied based on the habitat depth of each foraminifera species. Linear sedimentation rates are about ~4 cm/kyr in the Holocene and 4-10 cm/kyr in the last glacial and deglaciation. No age reversals were identified among the 31 age-control points. Sediment mixing may smooth the geochemical record, and thus offsets the change in Δ^{199}Hg (Liu *et al.*, 2021). Modelling studies indicate that the impact of sediment mixing depends on mixing depth and linear sedimentation rate. For the site at the Shatsky Rise with high sedimentation rates, the sediment mixing would introduce an uncertainty no more than 2 ka in the timing of Δ^{199}Hg change, based on sediment mixing depths (less than 10 cm) from previous studies in nearby regions (Ota *et al.*, 2022; Zhu *et al.*, 2024). Given that our Δ^{199}Hg trend focuses on deglacial and Holocene timescale spanning several millennia, the age model uncertainty will not compromise the validity of the temporal trend of Δ^{199}Hg. ODP Site 1208, located at the same site as core KEC, provides the record of the warm Pliocene with an age

between 2.5 Ma and 3.8 Ma (Shipboard Scientific Party, 2002). The age model is tuned to the standard $\delta^{18}O$ of Lisiecki and Raymo (2005) by Venti and Billups (2012). Briefly, a high-resolution orbital-scale chronology is generated by placing tie points at every isotope-stage boundary in LR04 (Lisiecki and Raymo, 2005). Since this study treats the Site 1208 data as a Pliocene group, the age model with orbital-scale resolution is sufficient.

The Shatsky Rise in the North Pacific open ocean is a remote region far from the continental shelf, receiving minimal direct terrestrial input. Previous study indicates that its sedimentary organic matter is predominantly marine-sourced (Maeda *et al.*, 2002). During the studied interval, the north Pacific Ocean lacks deep-water formation at the studied depths (*e.g.,* 3.4 km). Instead, the deep water submerging the Shatsky Rise is formed by the mixing of water masses transported along the ocean conveyor belt. These features suggest that the Shatsky Rise sediment has the potential to provide valuable insights into global open ocean Hg cycling rather than reflecting local signals. Two typical climate states, which are the period since the LGM and the warm Pliocene (3.8–2.5 Ma), are studied. Since the LGM, the climate system experienced prominent warming, accompanied by increasing atmospheric CO_2 and a major adjustment of the oceanic and terrestrial environment (Schmitt *et al*., 2012; Rae *et al*., 2020). Similarly, the Pliocene is the most recent warm period compared to the last glacial-interglacial cycle, when permanent Northern Hemisphere Glaciation has not developed (Haywood and Valdes, 2006; Fedorov *et al*., 2013). Given that no large-scale volcanism existed during the studied periods, we hypothesized the variations in Hg concentration and isotope values are mainly driven by non-volcanic natural processes, such as changes in oceanic organic carbon cycle, atmospheric deposition, and terrestrial vegetation coverage.

Details on analytical methods

Total mercury (THg) measurement. Total mercury concentration in the bulk sample (THg) is measured by a direct mercury analyzer DMA-80 (Milestone) at the Center for Marine Geochemistry Research, State Key Laboratory for Mineral Deposit Research, Nanjing University (Qu *et al.*, 2021). The blanks of sample holders are measured before usage. The sample used in THg measurement is weighed by a six-digit balance. The reliability of measurement is tested by certified reference materials (CRMs), which show 86 ± 2 ng/g (n = 7) for MESS-4 with a reference value of 80 ± 6 ng/g, and 465 ± 6 ng/g (n = 7) for NIST 2702 with a reference value of 454 ± 18 ng/g. The relative standard deviation (RSD) of Hg concentration for replicate samples is less than 5 %.

Mercury isotope analysis. The Hg isotope ratio analysis was performed in the School of Earth System Science, Tianjin University following the method of Enrico *et al*. (2021) and Sun *et al*. (2020). The oxidizing solution used to trap the elemental gaseous Hg is the 40 % inverse aqua regia. Before isotope analysis by a multi-collector inductively coupled plasma mass spectrometry (MC-ICP-MS, Nu Plasma 3D) coupled with a customized cold vapour generation system, the trapping solution was diluted to Hg concentration of ~1 ng ml^{-1}. The mass bias of the MC-ICP-MS was corrected by the NIST SRM 3133 Hg standard solution using the standard-sample bracketing method and the internal standard NIST SRM 997 Tl standard solution using the exponential law.

The secondary standard NIST SRM 8610 was analyzed between every five samples to evaluate the analytical uncertainty and precision, which yielded mean ± 2 SD (n = 23) values of −0.55 ± 0.04 ‰, −0.03 ± 0.04 ‰, 0.00 ± 0.04 ‰ for δ^{202}Hg, Δ^{199}Hg and Δ^{200}Hg, respectively. A marine sediment MESS-4 was used as procedural reference material to monitor the uncertainty of the whole sample preparation and analysis, which yielded mean ± 2 SD (n = 5) values of −1.79 ± 0.10 ‰, −0.01 ± 0.05 ‰, 0.02 ± 0.01 ‰, for δ^{202}Hg, Δ^{199}Hg and Δ^{200}Hg, respectively. The larger 2 SD uncertainties of Hg isotope ratios between NIST SRM 8610 and MESS-4 are used to represent the typical analytic uncertainties of Hg isotope ratios in our samples.

Total organic carbon (TOC) measurement. Total organic carbon (TOC) analysis was performed on a CNHS-O element combustion analyzer (Costech ECS 4024, NC Technologies) at the MOE Key Laboratory of Surficial Geochemistry, Nanjing University. About 0.5 to 1 g milled sediment sample was weighed into a PE tube and reacted with 1 M HCl overnight to remove carbonate minerals. The remaining solid was washed to neutral pH and freeze-dried. The weight difference between the decarbonated and the origin sample is calculated as the carbonate content. About 40 mg of freeze-dried decarbonated sample was warped into a tin cup to measure TOC. The RSD is less than 2 % for regular measurement. For samples with extremely low TOC content, the RSD rose to 5 % when the organic carbon input for measurement was 40 μg based on repeated measurement on 0.1 mg methionine as an external standard.

Sequential extraction of Fe-Mn oxide and major element concentration measurement. Sequential extraction was performed on the sediment based on the procedure of Poulton and Canfield (2005). Carbonate is first removed by 1 M sodium acetate (adjusted with acetic acid to pH 4.5) at room temperature for 24 h. Authigenic Fe and Mn were extracted by 1 M hydroxylamine-HCl in 25 % v/v acetic acid at room temperature for 48 h. Between extraction steps, the solid was washed with Milli-Q water for three times. The concentrations of major elements of the resulting extraction solution were measured by Thermo iCap 6000 Inductively Coupled Plasma Optical Emission Spectrometry (ICP-OES) at the MOE Key Laboratory of Surficial Geochemistry, Nanjing University. The RSD is less than 10 % for ICP-OES measurement.

The simplified time-dependent atmosphere-terrestrial-ocean box model. The Hg isotope box model is adapted from previous models (Sun *et al.*, 2019, 2023) and comprises five fully-coupled Hg reservoirs, including atmospheric (atmospheric Hg(0) and Hg(II)), terrestrial and oceanic (coastal and open ocean) reservoirs (Fig. S-1). Reservoir sizes, fluxes, and isotope fractionation factors are primarily from the published model (Sun *et al.*, 2023). The key parameters of this model are listed in Table S-2 and Table S-3. The external Hg input to the modelled system is from the deep mineral reservoir, including subaerial and submarine volcanic Hg emission, has fluxes and Δ^{199}Hg values of 300 Mg a^{-1} (Li *et al.*, 2020) and 0.00 ‰ (Moynier *et al.*, 2021), respectively. The total Hg burial flux is 600 Mg/yr in steady-state, which is equal to the sum of subaerial and submarine volcanic Hg emission, however, the relative contribution among terrestrial, coastal, and open ocean burial will change according to different model scenarios. The atmospheric Hg redox chemistry and atmospheric Hg(0)/Hg(II) partitioning in the model are assumed constant as modern

conditions (Amos *et al.*, 2013; Enrico *et al.*, 2017), as their evolution since the LGM remains poorly constrained (Murray *et al.*, 2014; Wang *et al.*, 2020).

The algorithm of the model is based on ordinary differential equations (ODEs) according to Hg mass balance and Hg isotope mass balance constraints (Sun *et al.*, 2019). The Hg mass transfer between reservoirs is controlled by first-order rate coefficients (k, year^{-1}, Table S-2), which is calculated as:

$$k_{j\to i} = \frac{F_{j\to i}}{M_j} \qquad \text{Eq. S-1}$$

where $F_{j\to i}$ (Mg/year) is the mass transfer flux of Hg from reservoir "j" to reservoir "i", and M_j (Mg) is the mass of Hg in reservoir "j". Based on the calculated rate coefficients, the Hg mass transfer is calculated by a group of 5 coupled ODE equations:

$$\frac{dM_i}{dt} = \sum_{j\neq i}\left(k_{j\to i} \times M_j\right) - \sum_{i\neq j}\left(k_{i\to j} \times M_i\right) + S \qquad \text{Eq. S-2}$$

where M_i and M_j (Mg) are the masses of Hg in reservoir "i" and "j". $k_{j\to i}$ and $k_{i\to j}$ are rate coefficients of Hg transfer fluxes from reservoir "j" to "i" and reservoir "i" to reservoir "j". S (Mg/year) is the external Hg input from the deep mineral reservoir.

Fractionation of Hg isotope odd-MIF (Δ^{199}Hg) between reservoirs are constrained by time-invariant Hg isotope enrichment factors (E^{199}), and are also calculated by a group of 5 coupled ODE equations:

$$\frac{dM_i \times \Delta^{199}Hg_i}{dt} = \sum_{j\neq i}\left[k_{j\to i} \times M_j \times \left(\Delta^{199}Hg_j + E^{199}Hg_{j\to i}\right)\right] - \sum_{i\neq j}\left[k_{i\to j} \times M_i \times \left(\Delta^{199}Hg_i + E^{199}Hg_{i\to j}\right)\right] + S \times \Delta^{199}Hg_S \qquad \text{Eq. S-3}$$

The E^{199} represent kinetic isotope fractionation as the Hg redox transformations are one-way kinetic processes. The time-step (dt) is small enough to avoid Rayleigh fractionation effect.

In this study, the rate coefficients are derived from the reservoir masses and fluxes of the well-known modern Hg cycle (Amos *et al.*, 2015; Horowitz *et al.*, 2017; Zhang *et al.*, 2023), and the calculated k values are listed in Table S-2. The E^{199} values used in this study (Table S-3) are based on published experimental results (Zheng and Hintelmann, 2009, 2010; Sun *et al.*, 2016) and tuned by previous modelling works (Sun *et al.*, 2019, 2023).

The model is prescribed to be in a steady state in both Hg flux and Δ^{199}Hg (*i.e.* input = output) using modern parameters without anthropogenic emission to reproduce the late Holocene state. In the late Holocene, terrestrial system mainly takes up atmospheric Hg(0), which contributes about 70 % of the terrestrial Hg fixation relative to ~30 % from atmospheric Hg(II) based on modern observations (Wang *et al.*, 2016a; Zhou *et al.*, 2021). To investigate the primary driver of the early Holocene Δ^{199}Hg increase, potential atmospheric, terrestrial, and marine processes are evaluated. Changes in atmospheric reactions, including Hg(0) oxidation and Hg(II) reduction, may alter the

atmospheric Δ^{199}Hg(0) and Δ^{199}Hg(II) signatures and, consequently, the Δ^{199}Hg signature of the open ocean. However, changes in the atmospheric oxidative capacity since the Last Glacial Maximum is complex, as indicated by existing modelling studies (Murray *et al.*, 2014; Wang *et al.*, 2020), and is poorly constrained due to a lack of observational record. Moreover, the effects of atmospheric physical and chemical changes on Hg MIF during Hg(0) oxidation and Hg(II) reduction are not well understood. Therefore, the atmospheric processes are assumed to remain consistent (constant rate coefficients and fractionation factors) following previous studies (Amos *et al.*, 2013; Enrico *et al.*, 2017). Based on this assumption, four processes that may have changed during the early Holocene and may have an influence on open ocean Δ^{199}Hg are considered in the modelling scenarios, including the uptake of atmospheric Hg(0) by terrestrial system (Figure 3), the precipitation of atmospheric Hg(II) to the open ocean, the particulate Hg burial in the open ocean, and the transport efficiency of coastal Hg to the open ocean (Fig. S-2). In these modelling scenarios, the relevant rate coefficient is set to change linearly from 11 ka to 6.5 ka to reproduce the observed Δ^{199}Hg shift during the early Holocene.

In scenario 1, $k_{atm\_Hg0\_tr}$ increases from 0.33 to 0.82 to model the open ocean Δ^{199}Hg increase by elevating the atmospheric Hg(0) uptake by terrestrial system. Under this scenario, the Hg(0) flux from the atmosphere to the terrestrial system increased by a factor of 1.7 during the early Holocene, which is consistent with an increase in terrestrial productivity by a factor of 1.43 to 2.00 (Prentice *et al.*, 2011; Ciais *et al.*, 2012). The increased terrestrial Hg pool will enhance the terrestrial sourced Hg burial with negative Δ^{199}Hg and facilitate the terrestrial Hg(0) emission causing increased atmospheric Δ^{199}Hg. Both the processes will lead to an increase in atmospheric and open ocean Δ^{199}Hg.

In scenario 2, $k_{atm\_Hg2\_open}$ increases from 1.38 to 3.94 to reproduce the open ocean Δ^{199}Hg increase by enhanced atmospheric Hg(II) deposition to the open ocean. In the atmosphere, the Hg(II) has a positive Δ^{199}Hg while the Hg(0) has negative values. In the open ocean system, higher proportion of atmospheric Hg(II) to Hg(0) deposition will result in a higher seawater Δ^{199}Hg. Although the hydrological cycle will be more active under warm climate (Lambert and Webb, 2008; Pendergrass, 2020), an increase in precipitation in open ocean by a factor of 2.4 is too large when compared to previous researches (Hancock *et al.*, 2023).

In scenario 3, $k_{open\_HgP\_sed}$ is decreased from 3.00×10^{-3} to 1.20×10^{-3} to model the open ocean Δ^{199}Hg increase caused by decreased open ocean particulate Hg burial. In the modelling system, decreased burial of open ocean Hg would cause an increase in Δ^{199}Hg values in the Earth's surface pools, while increased burial of terrestrial Hg would have an opposite effect. By decreasing the open ocean Hg burial, the surficial system Δ^{199}Hg will have a positive shift. However, the decrease of open ocean Hg burial by a factor of 0.6 during the early Holocene is not compatible with estimated TOC burial history (Cartapanis *et al.*, 2016), which suggests a rapid decrease of open ocean TOC during the deglaciation (about 17 to 11 ka) and tend to be stable during the early Holocene.

In scenario 4, the effect of increased continental shelf width caused by rising sea-level on open ocean Δ^{199}Hg is considered. The relevant rate coefficients including $k_{occ\_THg\_open}$ and $k_{open\_THg\_occ}$ are decreased from 12.76 to 3.19 and from 1.48×10^{-2} to 3.70×10^{-3}, respectively. The coastal ocean has a more negative Δ^{199}Hg than the open ocean, due to the terrestrial sourced Hg input by river discharge. The decreased connectivity between the coastal and open ocean caused by rising sea-level will thus result in a higher open ocean Δ^{199}Hg. To reproduce the observed open ocean Δ^{199}Hg increment, the coastal to open ocean Hg transport flux decreased by a factor of 0.33, in the meanwhile, the open ocean to coastal Hg transport flux decreased by a factor of 0.20. In the modelling scenario, water mass exchange between the coastal and open ocean during the early Holocene need to be markedly decreased during the early Holocene, when the open ocean Δ^{199}Hg increased. However, the sea-level rise starts at the beginning of the deglaciation (about 17.5 ka) (Stanford *et al.*, 2011; Yokoyama *et al.*, 2018). Considering the lack of tendency change of open ocean Δ^{199}Hg at the Shatsky Rise during the deglaciation and the clear increasing tend during the early Holocene, we suggest that the rising sea-level is not the main reason for the rising open ocean Δ^{199}Hg accompanied with the increasing atmospheric $\delta^{13}C_{atm}$.

Supplementary text on Hg isotope data

The mean δ^{202}Hg for core KEC is −0.51 ± 0.16 ‰ (2 SD, n = 25), and has no systematic changes during the last glacial-interglacial cycle. The Δ^{199}Hg shows a systematic increase during the early Holocene (11–8 ka), with the mean value during the glacial period (26–11 ka, Δ^{199}Hg = 0.16 ± 0.06 ‰, 2 SD, n = 14) significantly (unpaired Wilcoxon test, $p < 0.05$) lower than the mid to late Holocene (0-8 ka, Δ^{199}Hg = 0.21 ± 0.03 ‰, 2 SD, n = 5).

Note that a high resolution, glacial-interglacial resolved Δ^{199}Hg record for the Pliocene was not attempted here, as this would require a dedicated effort in a separate, focused study. We thus did not explore their temporal trend but treated all the isotope data as a single Pliocene group. The Pliocene Δ^{199}Hg and δ^{202}Hg data from Site 1208 are shown in Figure S-3 with THg, TOC and THg/TOC. The δ^{202}Hg ranges from -0.91‰ to -0.32‰ (mean = -0.57 ± 0.46 ‰, 2 SD, n = 11). The Δ^{199}Hg ranges from 0.14‰ to 0.30 ‰ (mean = 0.23 ± 0.08 ‰, 2 SD, n = 11). No correlation is observed between Δ^{199}Hg and THg/TOC. The average Δ^{199}Hg of Site 1208 samples is 0.06 ‰ higher (unpaired Wilcoxon test, $p < 0.05$) than that of core KEC samples (0.23 ‰ *vs.* 0.17 ‰).

During the warm Holocene, three Hg isotope data with low δ^{202}Hg and Δ^{199}Hg values coincide with periods of elevated bottom water oxygenation, suggesting additional Hg contributions. Similar low δ^{202}Hg and Δ^{199}Hg signatures have been observed in subsurface marine particles, likely linked to enhanced particulate organic matter (POM) degradation and microbial reworking (Jiskra *et al.*, 2021). Terrestrial Hg also exhibits highly negative δ^{202}Hg and Δ^{199}Hg signatures (Demers *et al.*, 2013; Wang *et al.*, 2022). During the deglacial period, the expansion of the North Pacific Subtropical Gyre (Yamamoto, 2005; Gray *et al.*, 2020) reduced nutrient supply at the site of core KEC, leading to lower productivity and potential shifts in biological communities (Amo and Minagawa, 2003; Ikehara *et al.*, 2009). Consequently, the sedimentary record may have become more susceptible to inputs of microbially reworked or

terrestrial POM during episodic events such as storms and stronger eddies (Manno *et al.*, 2015; Turner, 2015). Regardless of their exact origin, the anomalous data are confined to the late Holocene (8–0 ka) in the KEC record. We therefore suggest that the early Holocene (11–8 ka) Δ^{199}Hg increase still reflects the open ocean total Hg signal. As such, the three anomalous data are excluded from further discussion.

During deglacial, the expansion of the North Pacific Subtropical Gyre (Yamamoto, 2005; Gray *et al.*, 2020) reduced nutrient supply at the site of core KEC, leading to a shift to lower productivity and changes of biological communities (Amo and Minagawa, 2003; Ikehara *et al.*, 2009). Consequently, the sedimentary record may become more susceptible to inputs of refractory POM originated from biological degradation or terrestrial input during episodic events such as storms and stronger eddies (Manno *et al.*, 2015; Turner, 2015). Such refractory POM has less potential to exchange Hg with seawater, considering that the Hg exchange between POM and seawater is through a "regenerative scavenging" relying on POM degradation (Lamborg *et al.*, 2016). Regardless of their exact origin, the anomalous data are confined to the late Holocene (8–0 ka) in the KEC record. We therefore suggest that the early Holocene (11–8 ka) Δ^{199}Hg increase still reflects the open ocean Hg signal. As such, the three anomalous data are excluded from further discussion.

The Δ^{200}Hg exhibits no secular change under different climate states. The Δ^{200}Hg that is thought to be produced in the upper atmosphere (Chen *et al.*, 2012) has been widely used as a conservative tracer of atmospheric Hg deposition at the Earth's surface (Enrico *et al.*, 2016; Jiskra *et al.*, 2021; Song *et al.*, 2025). As shown in Figure S-4, MIF values of sediments for the Core KEC (26–0 ka) and Site ODP 1208 (3.8–2.5 Ma) lie closely within the Δ^{199}Hg vs Δ^{200}Hg mixing line of modern atmospheric Hg(0) and Hg(II) sources, considering the 95 % confidence interval. This suggests that the Δ^{199}Hg of our sediments mainly reflects the conservative mixing of Hg deposition from atmospheric Hg(0) and Hg(II), rather than odd-MIF processes within the water column, consistent with previous observations on other ocean basins (Jiskra *et al.*, 2021). Therefore, our open ocean sedimentary Δ^{199}Hg primarily reflects the source signatures of atmospheric Hg(0) and Hg(II) deposition.

Supplementary Tables

Table S-1 The Hg isotope data of Core KEC and Site 1208

ID	Depth	Age	δ^{202}Hg	δ^{202}Hg error 2SD	Δ^{199}Hg	Δ^{199}Hg error 2SD	Δ^{200}Hg	Δ^{200}Hg error 2SD	Δ^{201}Hg	Δ^{201}Hg error 2SD
KEC	**cmbsf**	**ka**	**‰**	**‰**	**‰**	**‰**	**‰**	**‰**	**‰**	**‰**
1	0	0.00	-0.55	0.10	0.23	0.05	0.00	0.01	0.19	0.06
2	4	1.97	-0.77	0.10	0.14	0.05	0.03	0.01	0.12	0.06
3	8	3.95	-0.84	0.10	0.11	0.05	0.01	0.01	0.14	0.06
4	10	4.94	-0.52	0.10	0.22	0.05	0.04	0.01	0.19	0.06
5	12	5.92	-0.38	0.10	0.20	0.05	0.03	0.01	0.17	0.06
6	14	6.51	-0.71	0.10	0.05	0.05	0.01	0.01	0.07	0.06
7	16	7.09	-0.50	0.10	0.20	0.05	0.04	0.01	0.20	0.06
8	18	7.67	-0.48	0.10	0.22	0.05	0.05	0.01	0.21	0.06
9	20	8.25	-0.44	0.10	0.19	0.05	0.05	0.01	0.15	0.06
10	22	8.84	-0.57	0.10	0.19	0.05	0.00	0.01	0.15	0.06
11	24	9.42	-0.59	0.10	0.18	0.05	0.03	0.01	0.19	0.06
12	28	10.19	-0.54	0.10	0.14	0.05	0.00	0.01	0.09	0.06
13	30	10.44	-0.51	0.10	0.16	0.05	0.01	0.01	0.16	0.06
14	32	10.78	-0.69	0.10	0.16	0.05	0.03	0.01	0.18	0.06
15	34	11.12	-0.36	0.10	0.15	0.05	0.02	0.01	0.13	0.06
16	42	12.73	-0.37	0.10	0.17	0.05	0.01	0.01	0.11	0.06
17	46	13.66	-0.54	0.10	0.18	0.05	0.04	0.01	0.12	0.06
18	50	14.60	-0.43	0.10	0.15	0.05	0.06	0.01	0.14	0.06
19	54	15.53	-0.42	0.10	0.12	0.05	0.02	0.01	0.20	0.06
20	62	16.75	-0.50	0.10	0.16	0.05	0.06	0.01	0.14	0.06
21	70	17.31	-0.60	0.10	0.12	0.05	0.03	0.01	0.18	0.06
22	78	18.26	-0.59	0.10	0.14	0.05	0.02	0.01	0.17	0.06
23	86	19.25	-0.58	0.10	0.21	0.05	0.05	0.01	0.15	0.06
24	94	19.91	-0.49	0.10	0.17	0.05	0.04	0.01	0.22	0.06

25	102	20.56	-0.41	0.10	0.18	0.05	0.05	0.01	0.14	0.06
26	122	22.08	-0.50	0.10	0.14	0.05	0.03	0.01	0.22	0.06
27	134	23.45	-0.44	0.10	0.12	0.05	0.04	0.01	0.18	0.06
28	146	25.26	-0.61	0.10	0.21	0.05	0.08	0.01	0.30	0.06
ODP 1208	**mbsf**	**ka**	**‰**	**‰**	**‰**	**‰**	**‰**	**‰**	**‰**	**‰**
29	117.8	2535	-0.91	0.10	0.14	0.05	0.02	0.01	0.10	0.06
30	121.2	2614	-0.38	0.10	0.24	0.05	0.06	0.01	0.17	0.06
31	122.1	2636	-0.32	0.10	0.20	0.05	0.02	0.01	0.20	0.06
32	128.5	2803	-0.34	0.10	0.22	0.05	0.04	0.01	0.20	0.06
33	135.6	2987	-0.48	0.10	0.30	0.05	0.06	0.01	0.24	0.06
34	138.4	3060	-0.38	0.10	0.23	0.05	0.02	0.01	0.26	0.06
35	144.3	3219	-0.70	0.10	0.27	0.05	0.03	0.01	0.24	0.06
36	145.1	3247	-0.55	0.10	0.23	0.05	0.05	0.01	0.24	0.06
37	147.9	3316	-0.81	0.10	0.28	0.05	0.04	0.01	0.21	0.06
38	155.5	3541	-0.91	0.10	0.18	0.05	0.05	0.01	0.17	0.06
39	157.1	3595	-0.46	0.10	0.22	0.05	0.04	0.01	0.16	0.06

Table S-2 First-order rate coefficients (k) used in the box model

Description of the reservoirs and fluxes	Variable name	Rate coefficient ($year^{-1}$)
Atmosphere		
Hg(0) oxidation to Hg(II)	$k_{atm\_Hg0\_Hg2}$	4.34
Hg(II) reduction to Hg(0)	$k_{atm\_Hg2\_Hg0}$	26.25
Hg(0) deposition to terrestrial system	$k_{atm\_Hg0\_tr}$	0.82 (0-6.5 ka) 0.33 (before 11 ka)
Hg(II) deposition to terrestrial system	$k_{atm\_Hg2\_tr}$	2.80
Hg(0) deposition to coastal ocean	$k_{atm\_Hg0\_occ}$	0.02
Hg(II) deposition to coastal ocean	$k_{atm\_Hg2\_occ}$	0.63
Hg(0) deposition to open ocean	$k_{atm\_Hg0\_open}$	0.45
Hg(II) deposition to open ocean	$k_{atm\_Hg2\_open}$	3.94 (0-6.5 ka) 1.38 (before 11 ka)

Terrestrial reservoir		
Hg(0) emission to atmosphere (nonphoto-)	$k_{tr\_Hg0\_atm\_res}$	1.50E-03
Hg(0) emission to atmosphere (photo-)	$k_{tr\_Hg0\_atm\_pr}$	9.87E-04
Hg(0) emission to atmosphere (re-emission)	$k_{tr\_Hg0\_atm\_r}$	7.87E-04
Hg(0) emission to atmosphere (biomass burning)	k_{tr_bb}	4.20E-04
Total Hg to coastal oceans by river discharge	k_{tr_riv}	3.10E-03
Terrestrial Hg burial	k_{tr_m}	4.20E-04
Coastal ocean		
Hg(0) evasion to atmosphere	$k_{occ\_Hg0\_atm}$	0.50
Total Hg transport to open ocean	$k_{occ\_THg\_open}$	3.19 (0-6.5 ka) 12.76 (before 11 ka)
Hg(P) sedimentation to coastal ocean floor	$k_{occ\_HgP\_sed}$	0.68
Open ocean		
Hg(0) evasion to atmosphere	$k_{open\_Hg0\_atm}$	0.02
Total Hg transport to coastal ocean	$k_{open\_THg\_occ}$	3.70E-03 (0-6.5 ka) 1.48E-02 (before 11 ka)
Hg(P) sedimentation to open ocean floor	$k_{open\_HgP\_sed}$	1.20E-03 (0-6.5 ka) 3.00E-03 (before 11 ka)

Note: The rate coefficients are calculated from modern Hg pools and fluxes shown in Figure S-1. Rate coefficients that are changed in the three modelling scenarios are listed with two values with time ranges.

Table S-3 The Hg isotope odd-MIF (Δ^{199}Hg) enrichment factors used in this study

Reactant	Product	Process	E^{199}
Hg^0 (g)	Hg^{II} (g)	Hg^0 oxidation in the atmosphere	−0.25
Hg^{II} (g)	Hg^0 (g)	Hg^{II} reduction in the atmosphere	−1.05
Hg^{II} (aq)	Hg^0 (g)	Hg^{II} reduction in terrestrial system	1.55
Hg^{II} (aq)	Hg^0 (g)	Hg^{II} reduction in surface ocean	0.00

Supplementary Figures

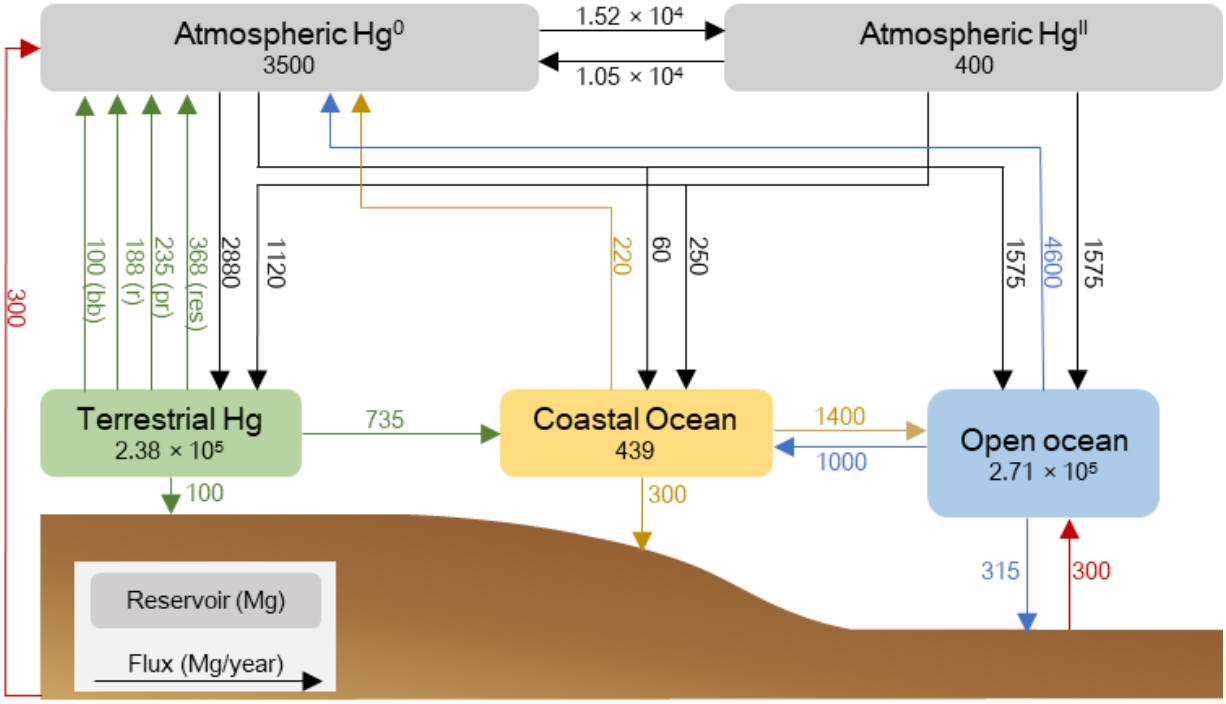

Figure S-1 The basic structure of simplified time-dependent atmosphere-terrestrial-ocean box model. The numbers in boxes and along arrows represent modern Hg reservoir sizes (Mg) and Hg transfer fluxes (Mg/year), respectively. The data are mostly from the previous box model (Sun *et al.*, 2023). The atmospheric Hg(0) and Hg(II) deposition flux on the ocean reservoirs are scaled down to achieve the high open ocean Δ^{199}Hg at the steady state; however, this would not affect the relative change of Δ^{199}Hg across different modelling scenarios. The multiple Hg mass transfer from one box to another by different processes are differentiated by arrows with processes identifiers (bb: biomass burning; r: re-emission; pr: photo emission; res: respiration). See Table S-1 for first-order rate coefficients calculated using reservoir sizes and fluxes of the modern state.

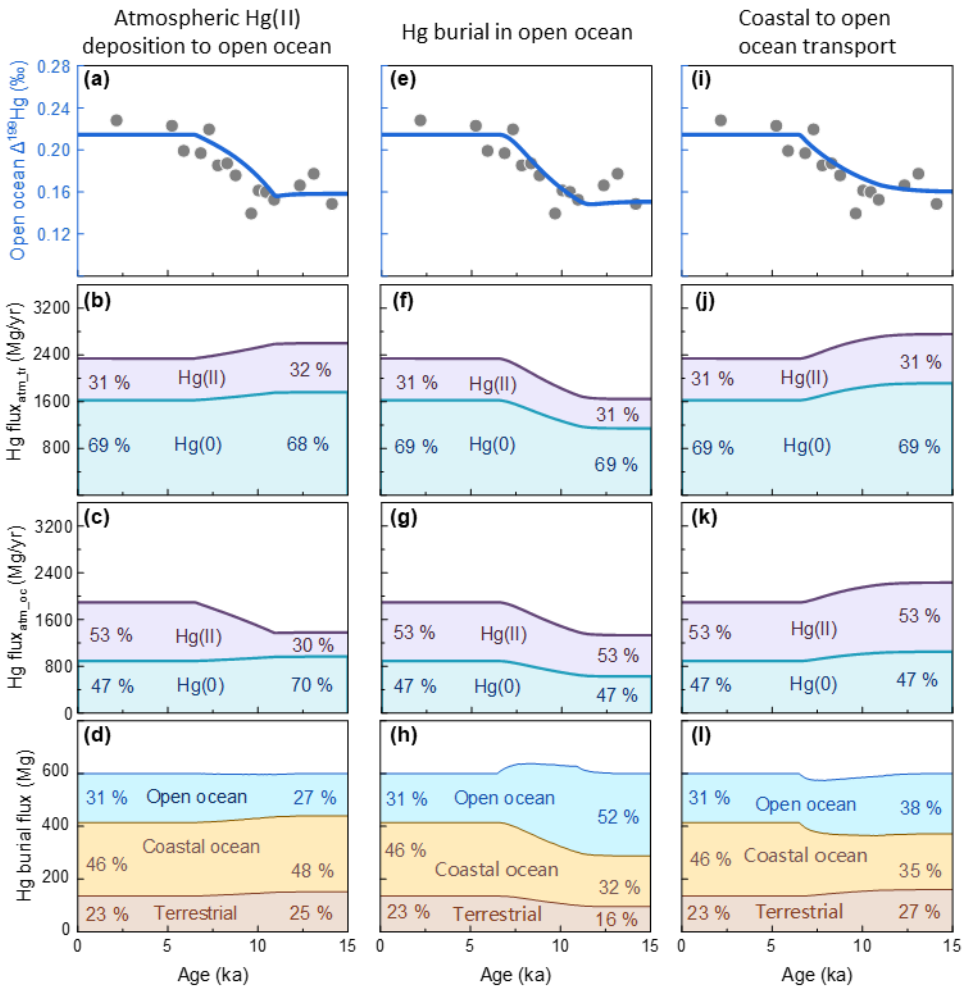

Figure S-2 Modelling outputs for the three alternative scenarios. Each column represents a distinct scenario, including increased atmospheric Hg(II) deposition to open ocean (a–d), decreased particulate Hg burial efficiency in the open ocean (e–h), and decreased coastal to open ocean transport (i–l). (a, e, i) The observed (grey points) and model output (blue lines) of the open ocean Δ^{199}Hg. (b, f, j) The atmospheric Hg deposition flux to the terrestrial system, with the blue and purple shades indicating Hg(0) and Hg(II) deposition flux, respectively. The percentages indicate the relative contribution of Hg(0) and Hg(II). (c, g, k) The atmospheric Hg deposition flux to the open ocean. The shades and percentages are the same as the second row. (d, h, l) The Hg burial flux and the burial ratio through terrestrial (brown), coastal (yellow) and open ocean (blue) systems.

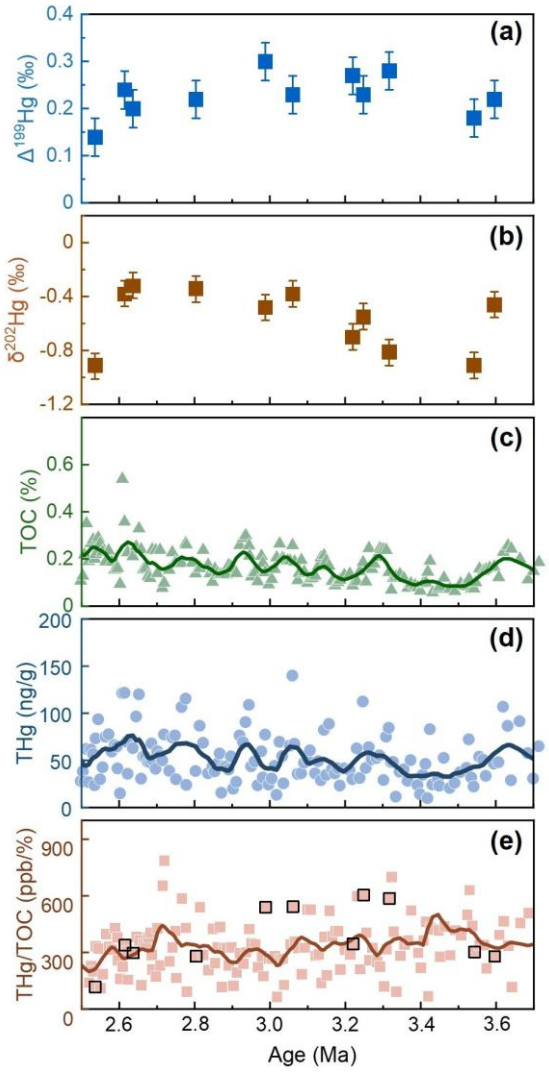

Figure S-3 Geochemical data of Site 1208 during the Pliocene. Time series of Δ^{199}Hg **(a)** and δ^{202}Hg **(b)**, as compared to TOC **(c)**, THg **(d)**, and THg/TOC ratio **(e)** in the main text. The grey shaded areas in **(a)** and **(b)** indicate Hg isotope ranges for core KEC. The black edged symbols in **(e)** indicate the samples with Hg isotope data.

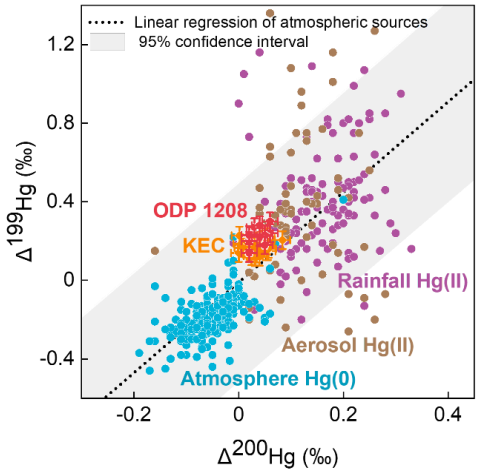

Figure S-4 The Δ^{199}Hg vs Δ^{200}Hg plot of sediment and atmospheric sources. The global rainfall Hg(II), aerosol Hg(II), and atmosphere Hg(0) are shown by purple, brown, and blue symbols (Jiskra *et al.*, 2021), respectively. The mixing of Hg(0) and Hg(II) sources is indicated by the linear regression line bounded by the 95% confidence interval (grey shade). Sediment data of Core KEC and Site ODP 1208 are shown in orange and red symbols, respectively.

Supplementary Information References

Amo, M., Minagawa, M. (2003) Sedimentary record of marine and terrigenous organic matter delivery to the Shatsky Rise, western North Pacific, over the last 130 kyr. *Organic Geochemistry* 34, 1299–1312. https://doi.org/10.1016/S0146-6380(03)00113-X

Amos, H.M., Jacob, D.J., Streets, D.G., Sunderland, E.M. (2013) Legacy impacts of all-time anthropogenic emissions on the global mercury cycle. *Global Biogeochemical Cycles* 27, 410–421. https://doi.org/10.1002/gbc.20040

Amos, H.M., Sonke, J.E., Obrist, D., Robins, N., Hagan, N., Horowitz, H.M., Mason, R.P., Witt, M., Hedgecock, I.M., Corbitt, E.S., Sunderland, E.M. (2015) Observational and modeling constraints on global anthropogenic enrichment of mercury. *Environmental Science & Technology* 49, 4036–4047. https://doi.org/10.1021/es5058665

Cartapanis, O., Bianchi, D., Jaccard, S.L., Galbraith, E.D. (2016) Global pulses of organic carbon burial in deep-sea sediments during glacial maxima. *Nature Communications* 7, 10796. https://doi.org/10.1038/ncomms10796

Chen, J., Hintelmann, H., Feng, X., Dimock, B. (2012) Unusual fractionation of both odd and even mercury isotopes in precipitation from Peterborough, ON, Canada. *Geochimica et Cosmochimica Acta* 90, 33–46. https://doi.org/10.1016/j.gca.2012.05.005

Ciais, P., Tagliabue, A., Cuntz, M., Bopp, L., Scholze, M., Hoffmann, G., Lourantou, A., Harrison, S.P., Prentice, I.C., Kelley, D.I., Koven, C., Piao, S.L. (2012) Large inert carbon pool in the terrestrial biosphere during the Last Glacial Maximum. *Nature Geoscience* 5, 74–79. https://doi.org/10.1038/ngeo1324

Demers, J.D., Blum, J.D., Zak, D.R. (2013) Mercury isotopes in a forested ecosystem: Implications for air-surface exchange dynamics and the global mercury cycle. *Global Biogeochemical Cycles* 27, 222–238. https://doi.org/10.1002/gbc.20021

Enrico, M., Roux, G. Le, Marusczak, N., Heimbürger, L.-E., Claustres, A., Fu, X., Sun, R., Sonke, J.E. (2016) Atmospheric Mercury Transfer to Peat Bogs Dominated by Gaseous Elemental Mercury Dry Deposition. *Environmental Science & Technology* 50, 2405–2412. https://doi.org/10.1021/acs.est.5b06058

Enrico, M., Le Roux, G., Heimbürger, L.-E., Van Beek, P., Souhaut, M., Chmeleff, J., Sonke, J.E. (2017) Holocene Atmospheric Mercury Levels Reconstructed from Peat Bog Mercury Stable Isotopes. *Environmental Science & Technology* 51, 5899–5906. https://doi.org/10.1021/acs.est.6b05804

Enrico, M., Balcom, P., Johnston, D.T., Foriel, J., Sunderland, E.M. (2021) Simultaneous combustion preparation for mercury isotope analysis and detection of total mercury using a direct mercury analyzer. *Analytica Chimica Acta* 1154, 338327. https://doi.org/10.1016/j.aca.2021.338327

Fedorov, A.V., Brierley, C.M., Lawrence, K.T., Liu, Z., Dekens, P.S., Ravelo, A.C. (2013) Patterns and mechanisms of early Pliocene warmth. *Nature* 496, 43–49. https://doi.org/10.1038/nature12003

Gray, W.R., Wills, R.C.J., Rae, J.W.B., Burke, A., Ivanovic, R.F., Roberts, W.H.G., Ferreira, D., Valdes, P.J. (2020) Wind-Driven Evolution of the North Pacific Subpolar Gyre Over the Last Deglaciation. *Geophysical Research Letters* 47, e2019GL086328. https://doi.org/10.1029/2019GL086328

Hancock, C.L., McKay, N.P., Erb, M.P., Kaufman, D.S., Routson, C.R., Ivanovic, R.F., Gregoire, L.J., Valdes, P. (2023) Global Synthesis of Regional Holocene Hydroclimate Variability Using Proxy and Model Data. *Paleoceanography and Paleoclimatology* 38, e2022PA004597. https://doi.org/10.1029/2022PA004597

Haywood, A.M., Valdes, P.J. (2006) Vegetation cover in a warmer world simulated using a dynamic global vegetation model for the Mid-Pliocene. *Palaeogeography, Palaeoclimatology, Palaeoecology* 237, 412–427. https://doi.org/10.1016/j.palaeo.2005.12.012

Horowitz, H.M., Jacob, D.J., Zhang, Y., Dibble, T.S., Slemr, F., Amos, H.M., Schmidt, J.A., Corbitt, E.S., Marais, E.A., Sunderland, E.M. (2017) A new mechanism for atmospheric mercury redox chemistry: implications for the global mercury budget. *Atmospheric Chemistry and Physics* 17, 6353–6371. https://doi.org/10.5194/acp-17-6353-2017

Ikehara, M., Akita, D., Matsuda, A. (2009) Enhanced marine productivity in the Kuroshio region off Shikoku during the last glacial period inferred from the accumulation and carbon isotopes of sedimentary organic matter. *Journal of Quaternary Science* 24, 848–855. https://doi.org/10.1002/jqs.1361

Jiskra, M., Heimbürger-Boavida, L.E., Desgranges, M.M., Petrova, M.V., Dufour, A., Ferreira-Araujo, B., Masbou, J., Chmeleff, J., Thyssen, M., Point, D., Sonke, J.E. (2021) Mercury stable isotopes constrain atmospheric sources to the ocean. *Nature* 597, 678–682. https://doi.org/10.1038/s41586-021-03859-8

Lambert, F.H., Webb, M.J. (2008) Dependency of global mean precipitation on surface temperature. *Geophysical Research Letters* 35, L16706. https://doi.org/10.1029/2008GL034838

Lamborg, C.H., Hammerschmidt, C.R., Bowman, K.L. (2016) An examination of the role of particles in oceanic mercury cycling. *Philosophical Transactions of the Royal Society A: Mathematical, Physical and Engineering Sciences* 374, 20150297. https://doi.org/10.1098/rsta.2015.0297

Li, C., Sonke, J.E., Le Roux, G., Piotrowska, N., Van Der Putten, N., Roberts, S.J., Daley, T., Rice, E., Gehrels, R., Enrico, M., Mauquoy, D., Roland, T.P., De Vleeschouwer, F. (2020) Unequal Anthropogenic Enrichment of Mercury in Earth's Northern and Southern Hemispheres. *ACS Earth and Space Chemistry* 4, 2073–2081. https://doi.org/10.1021/acsearthspacechem.0c00220

Lisiecki, L.E., Raymo, M.E. (2005) A Pliocene-Pleistocene stack of 57 globally distributed benthic δ 18O records. *Paleoceanography* 20, PA1003. https://doi.org/10.1029/2004PA001071

Liu, H., Meyers, S.R., Marcott, S.A. (2021) Unmixing deep-sea paleoclimate records: A study on bioturbation effects through convolution and deconvolution. *Earth and Planetary Science Letters* 564, 116883. https://doi.org/10.1016/j.epsl.2021.116883

Lougheed, B.C., Obrochta, S.P. (2019) A Rapid, Deterministic Age-Depth Modeling Routine for Geological Sequences With Inherent Depth Uncertainty. *Paleoceanography and Paleoclimatology* 34, 122–133. https://doi.org/10.1029/2018PA003457

Maeda, L., Kawahata, H., Nohara, M. (2002) Fluctuation of biogenic and abiogenic sedimentation on the Shatsky Rise in the western North Pacific during the late Quaternary. *Marine Geology* 189, 197–214. https://doi.org/10.1016/S0025-3227(02)00405-X

Manno, C., Stowasser, G., Enderlein, P., Fielding, S., Tarling, G.A. (2015) The contribution of zooplankton faecal pellets to deep-carbon transport in the Scotia Sea (Southern Ocean). *Biogeosciences* 12, 1955–1965. https://doi.org/10.5194/bg-12-1955-2015

Moynier, F., Jackson, M.G., Zhang, K., Cai, H., Halldórsson, S.A., Pik, R., Day, J.M.D., Chen, J. (2021) The Mercury Isotopic Composition of Earth's Mantle and the Use of Mass Independently Fractionated Hg to Test for Recycled Crust. *Geophysical Research Letters* 48, e2021GL094301. https://doi.org/10.1029/2021GL094301

Murray, L.T., Mickley, L.J., Kaplan, J.O., Sofen, E.D., Pfeiffer, M., Alexander, B. (2014) Factors controlling variability in the oxidative capacity of the troposphere since the Last Glacial Maximum. *Atmospheric Chemistry and Physics* 14, 3589–3622. https://doi.org/10.5194/acp-14-3589-2014

Ota, Y., Suzumura, M., Tsukasaki, A., Suzuki, A., Seike, K., Minatoya, J. (2022) Sediment accumulation rates and particle mixing at northwestern Pacific seamounts. *Journal of Marine Systems* 229, 103719. https://doi.org/10.1016/j.jmarsys.2022.103719

Pendergrass, A.G. (2020) The Global-Mean Precipitation Response to CO_2-Induced Warming in CMIP6 Models. *Geophysical Research Letters* 47, e2020GL089964. https://doi.org/10.1029/2020GL089964

Poulton, S.W., Canfield, D.E. (2005) Development of a sequential extraction procedure for iron: implications for iron partitioning in continentally derived particulates. *Chemical Geology* 214, 209–221. https://doi.org/10.1016/j.chemgeo.2004.09.003

Prentice, I.C., Harrison, S.P., Bartlein, P.J. (2011) Global vegetation and terrestrial carbon cycle changes after the last ice age. *New Phytologist* 189, 988–998. https://doi.org/10.1111/j.1469-8137.2010.03620.x

Qu, Y., Xu, K., Li, T., Wang, M., Zhong, H., Chen, T. (2021) Deep-sea coral evidence for dissolved mercury evolution in the deep North Pacific Ocean over the last 700 years. *Journal of Oceanology and Limnology* 39, 1622–1633. https://doi.org/10.1007/s00343-021-0474-6

Rae, J.W.B., Gray, W.R., Wills, R.C.J., Eisenman, I., Fitzhugh, B., Fotheringham, M., Littley, E.F.M., Rafter, P.A., Rees-Owen, R., Ridgwell, A., Taylor, B., Burke, A. (2020) Overturning circulation, nutrient limitation, and warming in the Glacial North Pacific. *Science Advances* 6, eabd1654. https://doi.org/10.1126/sciadv.abd1654

Schmitt, J., Schneider, R., Elsig, J., Leuenberger, D., Lourantou, A., Chappellaz, J., Köhler, P., Joos, F., Stocker, T.F., Leuenberger, M., Fischer, H. (2012) Carbon Isotope Constraints on the Deglacial CO_2 Rise from Ice Cores. *Science* 336, 711–714. https://doi.org/10.1126/science.1217161

Shipboard Scientific Party (2002) Site 1208. *Proceedings of the Ocean Drilling Program, 198 Initial Reports*, 1–93. https://doi.org/10.2973/odp.proc.ir.198.104.2002

Song, Z., Huang, S., Wang, Y., Zhang, P., Yuan, T., Tang, K., Fu, X., Zhang, Y. (2025) Atmospheric source of mercury to the ocean constrained by isotopic model. *Nature Communications* 16, 5752. https://doi.org/10.1038/s41467-025-60981-1

Stanford, J.D., Hemingway, R., Rohling, E.J., Challenor, P.G., Medina-Elizalde, M., Lester, A.J. (2011) Sea-level probability for the last deglaciation: A statistical analysis of far-field records. *Global and Planetary Change* 79, 193–203. https://doi.org/10.1016/j.gloplacha.2010.11.002

Sun, G., Sommar, J., Feng, X., Lin, C.-J., Ge, M., Wang, W., Yin, R., Fu, X., Shang, L. (2016) Mass-Dependent and -Independent Fractionation of Mercury Isotope during Gas-Phase Oxidation of Elemental Mercury Vapor by Atomic Cl and Br. *Environmental Science & Technology* 50, 9232–9241. https://doi.org/10.1021/acs.est.6b01668

Sun, R., Yuan, J., Sonke, J.E., Zhang, Y., Zhang, T., Zheng, W., Chen, S., Meng, M., Chen, J., Liu, Y., Peng, X., Liu, C. (2020) Methylmercury produced in upper oceans accumulates in deep Mariana Trench fauna. *Nature Communications* 11, 3389. https://doi.org/10.1038/s41467-020-17045-3

Sun, R., Liu, Y., Sonke, J.E., Feifei, Z., Zhao, Y., Zhang, Y., Chen, J., Liu, C.-Q., Shen, S., Anbar, A.D., Zheng, W. (2023) Mercury isotope evidence for marine photic zone euxinia across the end-Permian mass extinction. *Communications Earth & Environment* 4, 159. https://doi.org/10.1038/s43247-023-00821-6

Sun, R., Jiskra, M., Amos, H.M., Zhang, Y., Sunderland, E.M., Sonke, J.E. (2019) Modelling the mercury stable isotope distribution of Earth surface reservoirs: Implications for global Hg cycling. *Geochimica et Cosmochimica Acta* 246, 156–173. https://doi.org/10.1016/j.gca.2018.11.036

Turner, J.T. (2015) Zooplankton fecal pellets, marine snow, phytodetritus and the ocean's biological pump. *Progress in Oceanography* 130, 205–248. https://doi.org/10.1016/j.pocean.2014.08.005

Venti, N.L., Billups, K. (2012) Stable-isotope stratigraphy of the Pliocene–Pleistocene climate transition in the northwestern subtropical Pacific. *Palaeogeography, Palaeoclimatology, Palaeoecology* 326–328, 54–65. https://doi.org/10.1016/j.palaeo.2012.02.001

Wang, M., Fu, Q., Solomon, S., White, R.H., Alexander, B. (2020) Stratospheric Ozone in the Last Glacial Maximum. *Journal of Geophysical Research: Atmospheres* 125, e2020JD032929. https://doi.org/10.1029/2020JD032929

Wang, X., Bao, Z., Lin, C.-J., Yuan, W., Feng, X. (2016a) Assessment of Global Mercury Deposition through Litterfall. *Environmental Science & Technology* 50, 8548–8557. https://doi.org/10.1021/acs.est.5b06351

Wang, X., Lin, C.J., Lu, Z., Zhang, H., Zhang, Y., Feng, X. (2016b) Enhanced accumulation and storage of mercury on subtropical evergreen forest floor: Implications on mercury budget in global forest

ecosystems. *Journal of Geophysical Research: Biogeosciences* 121, 2096–2109. https://doi.org/10.1002/2016JG003446

Wang, X., Yuan, W., Lin, C.-J., Feng, X. (2022) Mercury cycling and isotopic fractionation in global forests. *Critical Reviews in Environmental Science and Technology* 52, 3763–3786. https://doi.org/10.1080/10643389.2021.1961505

Yamamoto, M. (2005) Equatorward shift of the subarctic boundary in the northwestern Pacific during the last deglaciation. *Geophysical Research Letters* 32, L05609. https://doi.org/10.1029/2004GL021903

Yang, X., Hu, R., Chen, T. (2024) *Age model (v1) of sediment core KEC*. *Mendeley Data*, V1. https://doi.org/10.17632/ht2pjmh5cd.1

Yokoyama, Y., Esat, T.M., Thompson, W.G., Thomas, A.L., Webster, J.M., Miyairi, Y., Sawada, C., Aze, T., Matsuzaki, H., Okuno, J., Fallon, S., Braga, J., Humblet, M., Iryu, Y., Potts, D.C., Fujita, K., Suzuki, A., Kan, H. (2018) Rapid glaciation and a two-step sea level plunge into the Last Glacial Maximum. *Nature* 559, 603–607. https://doi.org/10.1038/s41586-018-0335-4

Zhang, Y., Zhang, P., Song, Z., Huang, S., Yuan, T., Wu, P., Shah, V., Liu, M., Chen, L., Wang, X., Zhou, J., Agnan, Y. (2023) An updated global mercury budget from a coupled atmosphere-land-ocean model: 40% more re-emissions buffer the effect of primary emission reductions. *One Earth* 6, 316–325. https://doi.org/10.1016/j.oneear.2023.02.004

Zheng, W., Hintelmann, H. (2009) Mercury isotope fractionation during photoreduction in natural water is controlled by its Hg/DOC ratio. *Geochimica et Cosmochimica Acta* 73, 6704–6715. https://doi.org/10.1016/j.gca.2009.08.016

Zheng, W., Hintelmann, H. (2010) Isotope Fractionation of Mercury during Its Photochemical Reduction by Low-Molecular-Weight Organic Compounds. *The Journal of Physical Chemistry A* 114, 4246–4253. https://doi.org/10.1021/jp9111348

Zhou, J., Obrist, D., Dastoor, A., Jiskra, M., Ryjkov, A. (2021) Vegetation uptake of mercury and impacts on global cycling. *Nature Reviews Earth & Environment* 2, 269–284. https://doi.org/10.1038/s43017-021-00146-y

Zhu Z., Yu H., Bianchi T. S., Lian E., Burnett W. C., Paytan A., Guo X., Zhao S., Zhuang G., Men W., Li S., Yu Z., Xu B. (2024) What Causes Excess Deepening of the Sediment Mixed Layer in the Deep Ocean? *Geophysical Research Letters* 51, e2024GL108928. https://doi.org/10.1029/2024GL108928